ISPRS Journal of Photogrammetry and Remote Sensing 202 (2023) 169–183

Contents lists available at ScienceDirect

ISPRS Journal of Photogrammetry and Remote Sensing

journal homepage: www.elsevier.com/locate/isprsjprs

Dynamic estimation of rice aboveground biomass based on spectral and spatial information extracted from hyperspectral remote sensing images at different combinations of growth stages

Tianyue Xu [a,b,c], Fumin Wang [a,b,c,*], Zhou Shi [a,b,c], Lili Xie [c], Xiaoping Yao [c]

[a] Institute of Applied Remote Sensing & Information Technology, Zhejiang University, Hangzhou 310058, China
[b] Key Laboratory of Agricultural Remote Sensing and Information System, Zhejiang University, Hangzhou 310058, China
[c] Ministry of Education Key Laboratory of Environmental Remediation and Ecological Health, Zhejiang University, Hangzhou 310058, China

ARTICLE INFO

Keywords:
Data fusion
Optical
Vegetative growth stages
Gray level co-occurrence matrix
Time series

ABSTRACT

Aboveground biomass (AGB) is an essential factor in rice ecological research. Optical variables (e.g. reflectivity and vegetation index (VI)) are widely adopted in monitoring AGB while spatial information (e.g. texture) is less introduced into research. Limited research is available regarding the impact on the monitoring accuracy caused by the utility of VI and texture in AGB estimation at different combinations of growth stages. To compare the improvements caused by the involvement of texture at different combinations of growth stages, a hyperspectral camera was mounted on an unmanned aerial vehicle (UAV) to obtain images of rice field during the early growth stages (including the tillering, jointing and booting stage) under five nitrogen levels over two years. Spectral and spatial information derived from images was utilized to compute VIs and textures at different combinations of growth stages. After analyzing their correlations with AGB, multiple stepwise regression (MSR) and multiple linear regression (MLR) techniques were employed to establish rice AGB models using vegetation index (VI), vegetation index combined with the corresponding-band texture (VI-CBT) and vegetation index combined with the full-band texture (VI-FBT). It was found that the models using VI and texture enhanced the capability of the conventional VI to estimate AGB at different combinations of growth stages. The combination of VI and FBT achieved the most accurate estimation, followed by the VI-CBT. Different combinations of growth stages had diverse responses to textures. Overall, the tillering stage had the maximum response to the involvement of textures, followed by the booting stage. Models using VI-CBT and VI-FBT significantly improved the AGB estimation at the booting and tillering stage, respectively. The monitoring accuracy of the jointing stage showed a slight response to the involvement of texture. At the multiple growth stages, the monitoring effect of the tillering-booting stages was significantly improved, followed by the jointing-booting stages either using the model based on VI-CBT or VI-FBT. Models using VI and texture tended to yield larger improvements on the error values at the extreme AGB levels. Near-infrared and red-edge bands were the sensitive bands to estimate rice AGB, and MEA, COR were favorable textures to monitor the AGB. This study quantified the model improvements of using VI and texture in rice AGB estimation at different combinations of growth stages, delivering guidance for timely and accurate rice management in the field.

1. Introduction

Rice is one of the most important grain crops in the world, feeding almost fifty percent of the world's population (Seck et al., 2012). Aboveground biomass (AGB), a typical indicator of crop physiological status, reflects the nutrient accumulation of rice (Li et al., 2020a). The AGB estimation can be used to provide guidance for rice yield in precision agriculture, which is of vital importance in maintaining global food security (Spiertz and Ewert, 2009).

Traditional methods for measuring AGB, such as filed surveys, are labor-intensive, time-consuming and destructive, which limit the efficiency of data collection (Freeman et al., 2007). Numerous models developed on satellite remote sensing have been applied to large-scale biomass estimation such as forest (Lucas et al., 2020), grassland (Fang

* Corresponding author at: Institute of Applied Remote Sensing and Information Technology, Zhejiang University, Hangzhou 310058, China.
E-mail address: wfm@zju.edu.cn (F. Wang).

https://doi.org/10.1016/j.isprsjprs.2023.05.021
Received 23 October 2022; Received in revised form 13 February 2023; Accepted 17 May 2023
Available online 20 June 2023

et al., 2018; Yang et al., 2018) and marsh (Chen et al., 2022), etc. However, these models cannot attain satisfactory performance on the field scale due to the limitation of cloud and resolution (Yue et al., 2019). The emerging availability of unmanned aerial vehicle (UAV) provides novel opportunities to obtain high-resolution remote sensing images with abundant crop surface information. Nowadays, UAVs have become an indispensable approach in precision agriculture management (Fu et al., 2021; Mukherjee et al., 2019). Hyperspectral sensors, as one of the mainstream optical sensors, have brought unprecedented conveniences to monitor crop growth (Numata et al., 2008; Prey and Schmidhalter, 2019). Hyperspectral images simultaneously contain rich textural and spectral information, owning more advantages over multispectral images (Guo et al., 2021). The narrow and continuous spectrum of hyperspectral remote sensing provides more choices for the selection of specific bands in the spectral and spatial dimension (Xu et al., 2022b; Zhang et al., 2021). More robust and diverse indices, which respond more sensitively to subtle changes in crops, can be developed based on the information derived from the hyperspectral images (Inoue et al., 2008; Fang et al., 2017).

Vegetation index (VI), a typical spectral parameter, plays a vital role in monitoring crop physiological conditions (Chao et al., 2019; Xu et al., 2022c). Considerable efforts have been conducted to explore the feasibility of using various VIs for monitoring crop growth in precision agriculture. For instance, numerous VIs have produced satisfactory performances in estimating rice (Zheng et al., 2019), wheat (Li et al., 2022), and potato AGB (Liu et al., 2022b), etc. Apart from the spectral information, the UAV images with high resolution also obtain rich spatial information, offering possibility for the utilization of texture (Zheng et al., 2020b). Texture is always employed to characterize the spatial information of the crop phenotype such as the size and shape of the plant leaves (Xu et al., 2022b). The complementary relationship between VI and texture provides additional spatial information to the only spectral information contained in the pure vegetation index (Zheng et al., 2019). Numerous previous studies have illustrated that the combination of spectral and spatial information exhibits satisfactory performances in monitoring crop growth, such as crop yield (Wang et al., 2021), leaf area index (Li et al., 2019), nitrogen status (Liu et al., 2018; Zheng et al., 2020a), etc.

The relationships between VI and AGB vary with the growth stages of rice, which make the models based on single growth stage have less strength in reflecting the rice growing characteristic of other growth stages (Zhou et al., 2017). Combining the information of more than one growth stage together to calculate multiple temporal VIs is confirmed to be conductive in monitoring crop growth (Wang et al., 2019). Multiple temporal VIs, integrating the spectral information of the canopy over periods and covering a wider range of sensitive bands, can reflect the plant growing traits and offer abundant useful information related to AGB (Zhou et al., 2017). Multiple temporal models developed by VIs are demonstrated to perform well in predicting crop yield (Wang et al., 2019; Wang et al., 2021), nitrogen status (Zheng et al., 2018) and crop stress (Liu et al., 2010), etc. Practically speaking, the textural features also changed with the development of the rice growth stages (Xu et al., 2022b). Rice textures exhibit different responses to the AGB change, bringing challenges to assess the capability of textures to characterize AGB at different combinations of growth stages. Few studies have explored the performance of using VI incorporated with texture at different combinations of growth stages in the rice AGB estimation. Additionally, selecting the appropriate growth stages to establish AGB models is of significant value for improving the monitoring accuracy and increasing the modelling efficiency (Qiu et al., 2020). Limited research is available regarding the rice AGB using multiple temporal VIs and textures.

Based on the statements mentioned above, the research combined the spectral and spatial information derived from the high-resolution UAV hyperspectral images of the tillering, jointing and booting stage to establish different temporal models using the vegetation index (VI), the vegetation index combined with the corresponding-band texture (VI-CBT), and the vegetation index combined with the full-band texture (VI-FBT), respectively. The main objectives of the study are thus to (1) assess the feasibility of using textures and VI derived from UAV hyperspectral images to improve AGB estimation; (2) compare the improvements of the monitoring accuracy caused by the involvement of texture at different combinations of growth stages; (3) assess the monitoring effects under varied AGB levels and judge the overestimations and underestimations of rice AGB.

2. Material and methods

2.1. Experimental design

The field experiments were conducted in the functional zone of grain production of Xiashe village, Deqing County, Huzhou City, Zhejiang Province, China (120°10′51.20″E, 30°34′21.00″N) from 2018 to 2019 (Fig. 1). The local natural conditions including the abundant heat and precipitation laid a solid foundation for rice planting experiments. The experiment site was divided into twenty micro-plots and assigned to five nitrogen treatments and two varieties each year. Zhejing 99 (S1) and Jia 67 (S2) were cultivated in 2018, and Nanjing 9108 (S1) and Nanjing 46 (S2) were planted in 2019. The rice intervals between holes were kept constant with a distance of 25 cm in the horizontal direction and 23 cm in the longitudinal direction. Twenty samples were selected during each growth stage annually.

Five nitrogen fertilization levels, including N0 (0% of the normal treatment), N1 (50% of the normal treatment), N2 (normal treatment), N3 (150% of the normal treatment) and N4 (200% of the normal treatment), were implemented on rice groups over the two years with the constant phosphate fertilization and potash fertilization. Each treatment was repeated twice among the twenty micro-plots.

2.2. Collection of the AGB data

An area of 2*2 plots was placed at the positions where the rice grew uniformly from south to north of the field to conduct repeated destructive samplings. The number of the rice plants in each sample was manually counted in an experimental room adjacent to the field. After cleaning the soil and stains on the plants with running water, the organs of the rice plants were separated and put into sealed bags immediately. After being dried at 105℃ for 40 minutes and then 65 ℃ until the constant mass in the oven, the dry mass of the leaves and stems were weighed by high precision balance. The sum of the dry mass and population density of the sample was used to calculate the total rice AGB in each plot. The formula for calculating the AGB is as follows:

$$\mathrm{AGB} = \frac{\text{Dry leaf weight} + \text{Stem weight}}{\text{Number of sampled plants}} \times \text{Stems per hectare} \quad (1)$$

2.3. Collection of the UAV-hyperspectral images

2.3.1. UAV images collection

A six-rotor UAV platform carrying a Rikola hyperspectral camera was adopted to collect high-resolution images on the same days of ground sampling (Fig. 2). The experimental route was pre-determined with a flying height of 200 m, resulting in 13 cm spatial resolution. Three fixed points were designed along the flight path and the camera was set to take images at an interval of 45 seconds automatically. The UAV-based platform equipped with the shock-absorbing design was carefully checked before each experiment to ensure stable flights and reliable data. All flights were conducted on clear, light days with calm weather and the UAV-based images were collected between 10:00 a.m -2:00p.m.

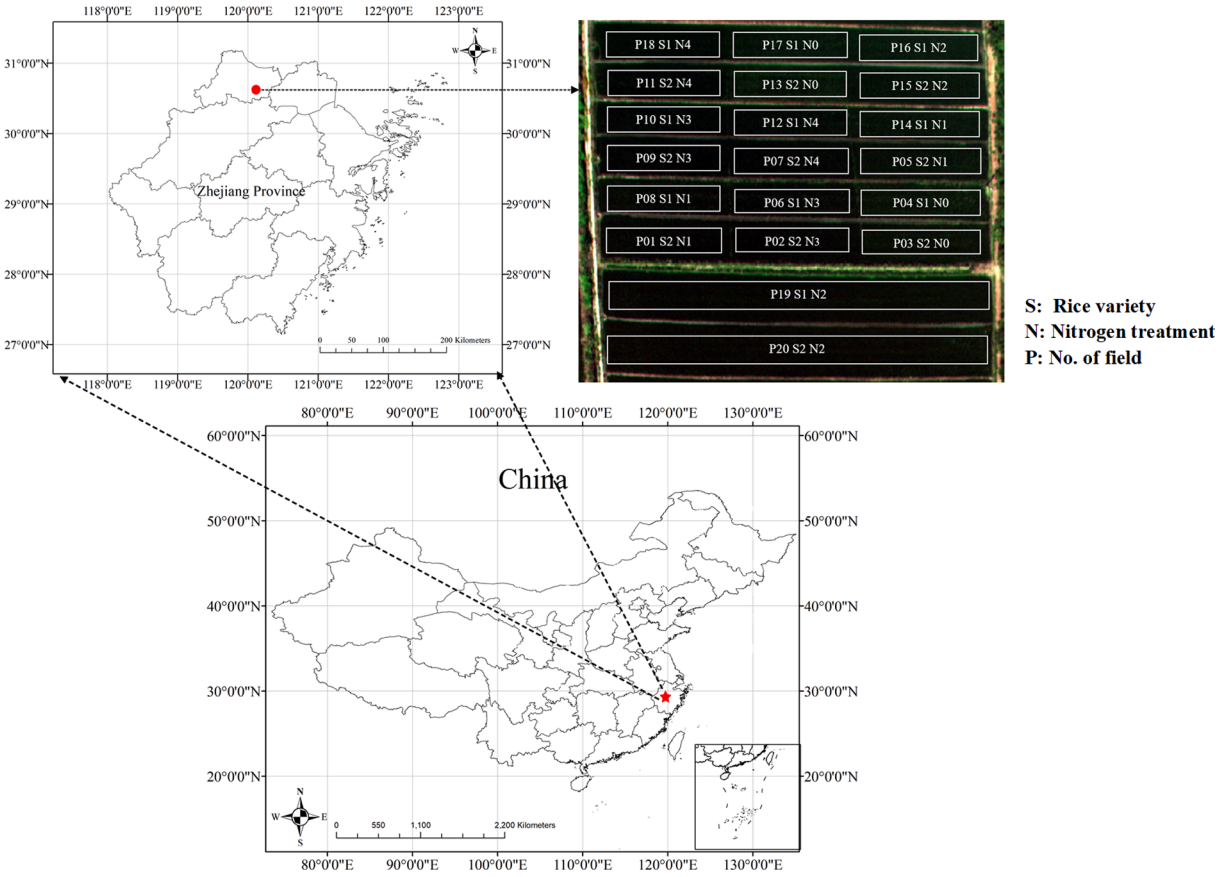

Fig. 1. The geographical location of experimental field and schematic diagram of field design.

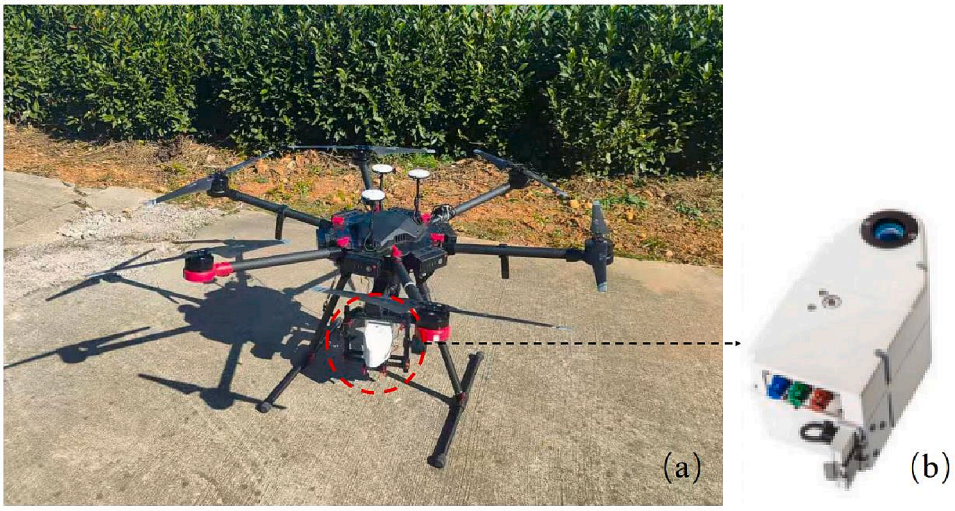

Fig. 2. UAV hyperspectral platform. (a) DJI M600 Pro UAV; (b) Rikola camera.

2.3.2. UAV images processing

Images stored on memory cards should be pre-processed before being put into use. Rikola hyperspectral imager V2.1.4 (Rikola Ltd., Oulu, Finland) was utilized for data conversion, lens correction, halo correction and dark current removal, adjusting the systemic errors and solving the problem of image deformation. RegMosaic (Rikola, Ltd.) software was employed to conduct band correction, refining the band shift caused by disparate imaging sequences. A diffuse gray cloth was utilized as a standard reference plate for the radiation correction. The reflectivity of the whole image shall be calculated by formula (2) in the ENVI software.

$$\mathrm{Ref}_{\mathrm{img}} = \frac{\mathrm{Rad}_{\mathrm{img}} \times \mathrm{Ref}_{\mathrm{gray}}}{\mathrm{Rad}_{\mathrm{gray}}} \tag{2}$$

where $\mathrm{Rad}_{\mathrm{img}}$ is the radiation value of the whole image, $\mathrm{Ref}_{\mathrm{img}}$ is the reflectivity of the whole image, $\mathrm{Rad}_{\mathrm{gray}}$ is the radiation value of the standard reference plate, and $\mathrm{Ref}_{\mathrm{gray}}$ is the reflectivity of the standard reference plate.

2.4. Extraction of remote sensing variables

2.4.1. Calculation of vegetation indices

A regular rectangle was drawn to establish the region of interest to obtain the average reflectivity in each plot. Three vegetation indices including NDVI type, RVI type and DVI type, which were widely confirmed to have positive relationships with rice growth, were selected to monitor the AGB (Table 1). The 62 bands ranging from 500 nm to 900 nm of the hyperspectral images were utilized to build VIs composed of all possible band combinations, taking full use of the abundant spectral information.

To take advantage of the hyperspectral images and select the representative band combinations, a deterministic approach was adopted to select ten typical VIs in each type: the correlation between the VIs composed of all possible combinations of bands and AGB together with their distributions on the contour maps were considered simultaneously. The optimal VIs with the local maximum correlation in various band ranges on the contour maps were selected. Selecting such indices ensured a great correlation with AGB and a low collinearity.

2.4.2. Calculation of textures

Gray level co-occurrence matrix algorithm (GLCM), a method proposed by R.Haralick in the 1970 s, was utilized to quantify the textural features (Haralick et al., 1973; Yokoyama and Haralick, 1978). The GLCMs interpret the spatial relationship between two pixels at a certain distance to reflect the gray-scale information of the images (Yokoyama and Haralick, 1979; Lumia et al., 1983; de Siqueira et al., 2013). Before calculating the GLCMs, the intensity values of each image needed to be compressed from 256 to 64 gray levels to reduce the computation time (Lu et al., 2019). The GLCMs were calculated in the 3 * 3 window and 5 * 5 window with a step length as one pixel, respectively. The average value of the two windows was taken as the final value to synthesize the advantages of the various windows. Eight textures including mean (MEA), variance (VAR), homogeneity (HOM), contrast (CON), dissimilarity (DIS), entropy (ENT), secondary moment (SEM) and correlation (COR) were computed in the rotation directions of 0°, 45°, 90° and 135°, respectively.

2.5. Construction and evaluation of models

A large number of bands of the UAV hyperspectral images inevitably result in the problem of data redundancy, bringing obstacles for data storage and calculation (Hsu, 2007). To identify the internal relationship between variables and AGB, multiple stepwise regression (MSR) was adopted to construct a reasonable mechanism of variable selection to avoid the autocorrelation between variables (Nakaji et al., 2014). The stepwise regression method took the forward–backward form, which means it continuously increased variables and simultaneously considered the possibility of the previously eliminated variables until the increase of variables no longer led to a significant reduction of sum of squared error (SSE) (Kokaly and Clark, 1999; Zhang, 2016). The modelling process was implemented in the Statistical Package for Social Science (SPSS) software (version 25.0, IBM Corporation, Armonk, NY, USA). Multiple linear regression (MLR) with high interpretability and good fitting degree was then employed to establish multifactor models (Chierici et al., 2012). They took the form of the following equation:

$$AGB = \beta_0 + \beta_1 X_1 + \beta_2 X_2 + \beta_3 X_3 + \cdots \beta_n X_n \quad (3)$$

where AGB is the estimated rice AGB based on the regression model, X_n stands for the independent variables and β_n stands for the coefficient of each variable.

Four evaluation indices, including the coefficient of determination (R^2), the root-mean-square error (RMSE), the relative root-mean-square error (rRMSE) and mean absolute percentage error (MAPE) were used to assess the model performance. R^2 stands for the fitting degree of the model, RMSE represents the degree of the dispersion of the samples. MAPE and rRMSE both belong to non-dimensional evaluation indicators, which measure the prediction accuracy of the model and are unaffected by the magnitude of variables. Generally, a model with a higher R^2 and lower RMSE, rRMSE and MAPE indicates that it has a higher accuracy (Agbulut et al., 2021).

$$R^2 = 1 - \frac{\sum_i (Y - Y')^2}{\sum_i (Y - \bar{Y})^2} \quad (4)$$

$$RMSE = \sqrt{\frac{\sum_{i=1}^{n} (Y - Y')^2}{n}} \quad (5)$$

$$rRMSE = \frac{RMSE}{\bar{Y}} \quad (6)$$

$$MAPE = \frac{100\%}{n} \sum_{i=1}^{n} \left| \frac{Y - Y'}{Y} \right| \quad (7)$$

where Y stands for the actual AGB, $\bar{Y}$ stands for the average value of the measured AGB and Y' stands for the estimated AGB.

In this study, the comprehensive data of two years was used to expand the data range of samples and integrate the AGB characteristics of different rice types, making the models more universal. VI, VI-CBT and VI-FBT were incorporated into the AGB models at different combinations of growth stages. First, MSR was required to select the remote sensing variables highly related to rice AGB. Second, MLR was employed to incorporate all influencing factors in establishing AGB models. Each dataset was divided into three groups evenly, with a calibration dataset with 2/3 data (e.g. 27 samples, 53 samples, 80 samples) and a validation dataset with 1/3 data (e.g. 13 samples, 27 samples, 40 samples) to test the stability of the models. The method not only ensured the rationality of data selection, making the calibration dataset and validation dataset better reflect the data distribution characteristics, but also made sure of the reliability of the established models.

The experimental workflow presented in Fig. 3 demonstrated the experiment methodology of the study, including the data collection, modelling process and result assessments. VIs, GLCM-based textures derived from the hyperspectral images were individual or combined to build models using VI, VI-CBT and VI-FBT and then compared their respective monitoring effect.

Table 1
Introduction of the selected VIs.

VI type	Index name	Formula	References
$NDVI_{(\lambda,\mu)}$	Normalized difference vegetation index	$(\rho_\lambda + \rho_\mu)/(\rho_\lambda - \rho_\mu)$	(Rouse et al., 1974)
$RVI_{(\lambda,\mu)}$	Ratio vegetation index	ρ_λ/ρ_μ	(Jordan, 1969)
$DVI_{(\lambda,\mu)}$	Difference vegetation index	$\rho_\lambda - \rho_\mu$	(Tucker, 1979)

Note: λ and μ represent the arbitrary band among the 62 bands in the hyperspectral images.

3. Results

3.1. Selection of remote sensing variables

3.1.1. Selection of the VIs

VIs, including multiple temporal VIs and single temporal VIs, were calculated by the reflectivity extracted from the images. Single temporal VIs were calculated based on the information from one-growth stage while multiple temporal VIs were computed by selecting the sensitive

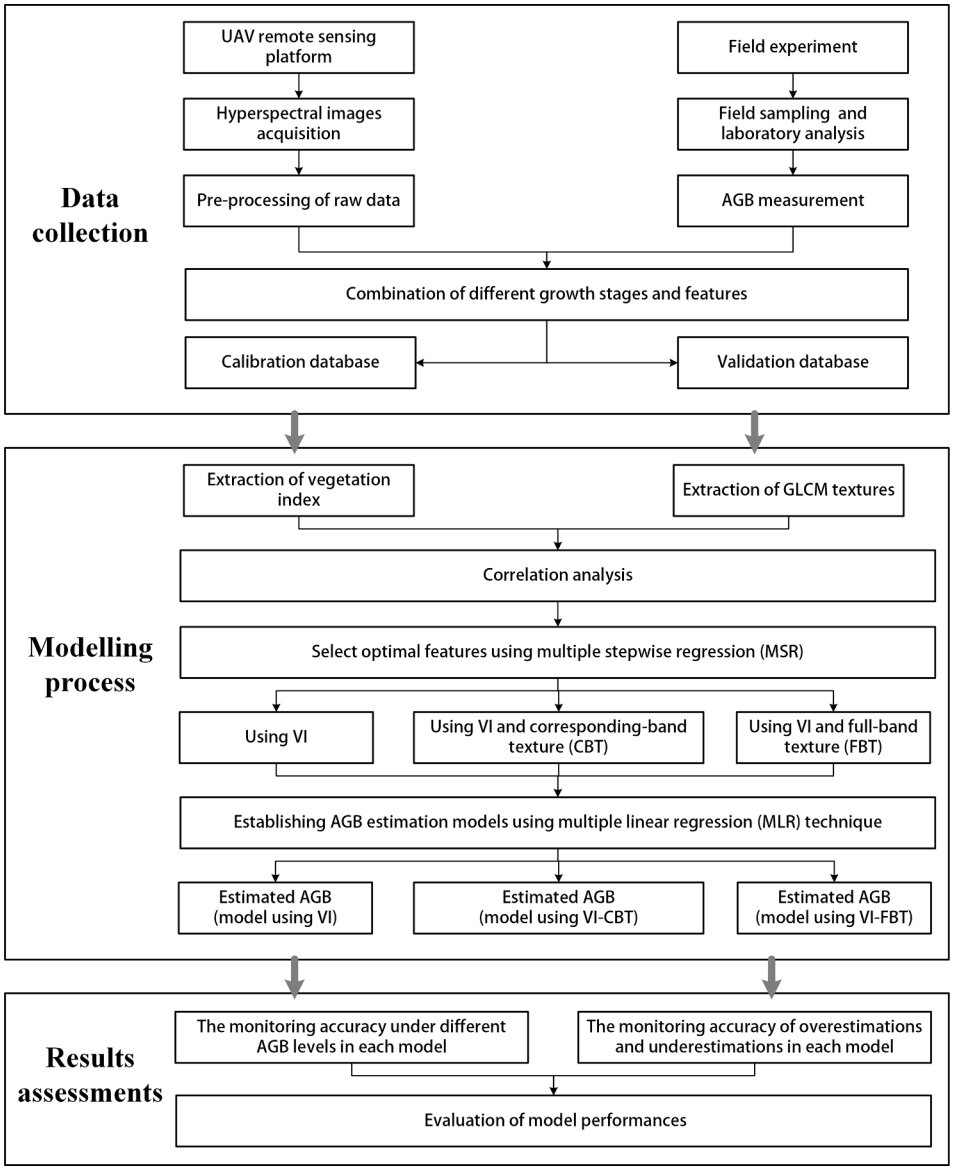

Fig. 3. Flowchart of the experimental method.

bands from the dataset composed of multiple growth stages (i.e. two-growth stage and three-growth stage). The coefficient of correlation (r) between the feature and the AGB was computed using the MATLAB R2021b (The MathWorks, Inc.), and the powerful visualization capabilities of MATLAB software were used to plot the contours map of the absolute value of r between the vegetation indices and rice AGB at different growth stages. The abscissa and ordinate correspond to the wavebands of the VIs, and the pixel values represent the absolute value of r between the VIs and AGB.

It can be observed that the band locations of the VIs highly correlated with AGB were inconsistent, and the correlations between VIs and AGB changed at different combinations of growth stages. The results demonstrated that red, red-edge and near-infrared spectral regions were of reasonable importance for AGB estimation. Yellow and green bands appeared to exhibit positive correlations with AGB in part of the growth stages, such as band one and band two ranging from 500 to 600 nm at the booting stages (NDVI, RVI). At single growth stage, the VIs of the tillering stage exhibited the highest overall correlations with AGB, followed by the booting and the jointing stage. At multiple growth stages, a majority of VIs of the tillering-booting stages had positive correlation with rice AGB ($r \geq 0.5$) (Fig. 4 and Fig. 5).

Ten vegetation indices were further selected within each type to service as the potential textures of establishing AGB models. The filtered band combinations of the selected vegetation indices were shown in Table 2.

3.1.2. *Selection of the textures*

Incorporating appropriate variables into the models can accelerate the modeling process (Zhao et al., 2013). The textures highly correlated with rice AGB were identified by MSR, and then the correlations between these textures and AGB were performed by Pearson correlation analysis. The statistical analysis showed that SEM_{600} of the booting stage stood out to have the strongest correlation with rice AGB (r=0.775), followed by MEA_{840} (r=0.683) of the tillering-booting stages and MEA_{656} of the tillering stage (r=-0.680). Textures were more likely to exhibit weak correlation with rice AGB at the tillering-jointing stages ($r \leq 0.3$). Most of the bands in the textures were located in the red, red-edge, and near-infrared spectral regions, while the yellow and green bands also appeared in some full-band textures, further broadening the wavelength range of textures (Table 3).

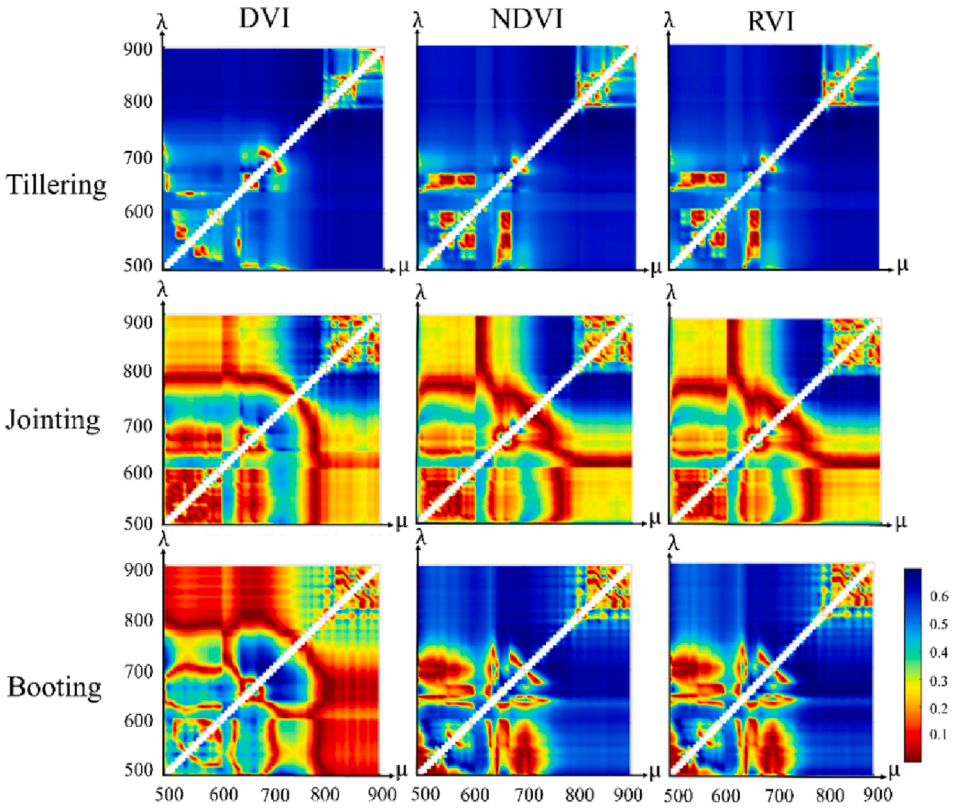

Fig. 4. Correlations between VIs and AGB at single growth stages.

3.2. Construction of rice AGB models at different growth stages

The seven kinds of combinations of growth stages were the all possible combinations of the three growth stages, and were then divided into one-growth stage dataset, two-growth stage dataset and three-growth stage dataset according to the included number of growth stages. Different temporal remote sensing variables including VI, VI-CBT and VI-FBT were utilized to establish models at these seven kinds of combinations of growth stage (Table 4). The basic principle of modeling was to ensure the ideal estimation accuracy and the least participating variables simultaneously, avoiding the redundancy and complexity of the models.

The types and bands of VIs and textures varied at different combinations of growth stages (Table 4). The rate of photosynthesis speeds up with the growth of rice plants from the tillering stage to the jointing stage (Xu et al., 2022b). The popularity of NDVI during the earlier rice growth stages (i.e. the tillering stage and jointing stage) was as expected, since it effectively illustrated the dynamic changes of pigments and nutrients of crop at low canopy coverage (Camps-Valls et al., 2021; Haboudane et al., 2004). Nevertheless, saturations of NDVI and DVI were likely to happen at the booting stage (Li et al., 2020b), hindering their reliability as effective indicators of AGB. RVI with the ability of anti-saturation gave light on the estimation of dense AGB (Yao et al., 2014). Therefore, RVI turned out to be increasingly crucial at the booting stage.

The frequent occurrences of near-infrared and red-edge bands in the models demonstrated that they were instructive for AGB estimation. The near-infrared bands have a stronger capability to penetrate the crop canopies and resist saturation than the visible bands when monitoring plant biological growth (Berard et al., 2017; Devia et al., 2019). Red-edge is the spectral region where a steep gradient appears at the boundary between the near-infrared and red bands (Sun et al., 2010). Red-edge bands, which can sensitively sense the changes of chlorophyll, have been proved to be effective to monitor crop development in the previous studies (Huang et al., 2017; Dong et al., 2020). VIs developed by the near-infrared and red-edge band, have been pointed out to be helpful for alleviating the radiation distractions caused by the atmospheric transmission, enhancing the capability to describe plant biophysical traits (Cao et al., 2013).

It is worth noting that the red shift phenomenon occurred as the red-edge band gradually expanded from 700 nm at the tillering stage to 748 nm at the jointing stage and 752 nm at the booting stage. The phenomenon possibly attributed to the fact that the increase of the chlorophyll content and leaf area resulted in the widened absorption zone of red-edge and the expanding amplitude of the red-edge, making the band move towards the longwave direction (Liu et al., 2020). Yellow and green bands only appeared in the textures, indicating that these bands might be more suitable for rice AGB estimation in the spatial dimension. This phenomenon is possibly related to the reason that yellow and green bands have less effect on photosynthesis, but have strong abilities to detect soil background (Meng et al., 2017). The frequent occurrences of MEA and COR in models signified that they were irreplaceable in rice AGB estimation, which agrees with the findings of the previous research (Lu et al., 2021; Xu et al., 2022b).

3.3. Evaluation of rice AGB models at single growth stage

Both on the calibration and validation datasets, the accuracy of using the combinations of VI and texture was higher than using VI alone, and the successive order of the monitoring accuracy from high to low was the models based on VI-FBT, VI-CBT, and VI (Tables 5–8).

At the tillering stage, the model using VI-CBT and VI-FBT significantly decreased the rRMSE by 6.355% and 41.425%, respectively in the calibration dataset, and dropped by 2.466% and 27.239%, respectively in the validation dataset at the tillering stage when compared to the model using VI. The monitoring accuracy was slightly improved by the involvement of texture at the jointing stage, with the MAPE only decreasing by 1.299% and 4.171% in the calibration dataset, and

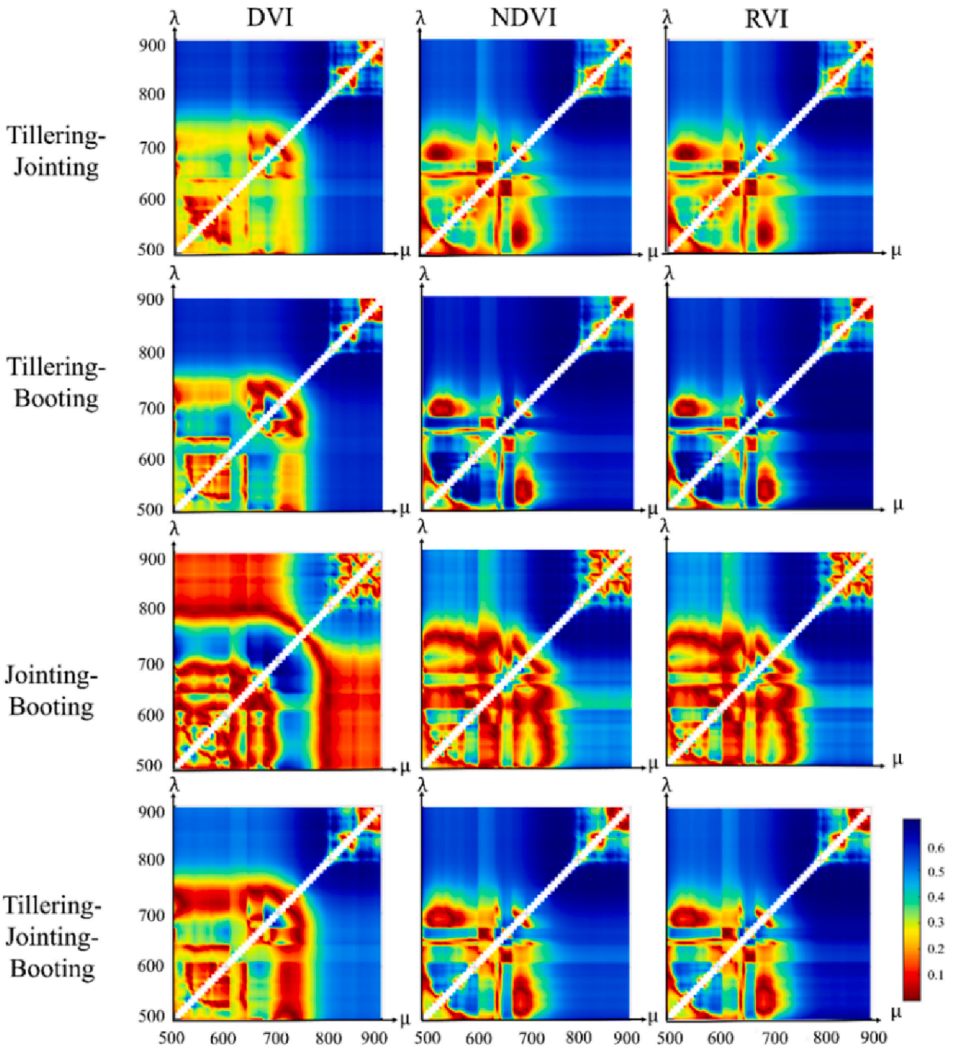

Fig. 5. Correlations between VIs and AGB at multiple growth stages.

Table 2
The filtered band combinations of the potential selected vegetation indices.

Stage	Index	Filtered band combination									
Tillering	DVI	[504,544]	[552,604]	[624,724]	[650,672]	[688,740]	[720,864]	[748,744]	[752,800]	[768,816]	[792,856]
	NDVI	[512,528]	[544,608]	[560,720]	[635,848]	[680,808]	[724,824]	[760,700]	[768,808]	[784,840]	[792,888]
	RVI	[504,536]	[536,616]	[568,728]	[632,856]	[672,824]	[728,700]	[740,808]	[768,840]	[784,864]	[792,880]
Jointing	DVI	[504,650]	[536,709]	[576,700]	[650,700]	[696,704]	[700,704]	[704,709]	[776,800]	[792,832]	[800,888]
	NDVI	[512,650]	[552,709]	[592,700]	[624,704]	[760,768]	[776,748]	[784,800]	[792,816]	[800,752]	[800,888]
	RVI	[512,635]	[544,704]	[592,709]	[632,704]	[752,768]	[768,848]	[784,800]	[792,808]	[800,808]	[800,888]
Booting	DVI	[504,512]	[552,604]	[576,580]	[584,688]	[616,696]	[650,584]	[685,600]	[692,709]	[709,712]	[800,888]
	NDVI	[504,784]	[552,808]	[592,888]	[624,784]	[650,808]	[688,712]	[709,704]	[744,888]	[784,808]	[792,856]
	RVI	[512,816]	[536,872]	[588,816]	[632,856]	[688,848]	[712,840]	[752,700]	[768,856]	[792,864]	[840,664]
Tillering- Jointing	DVI	[504,792]	[544,800]	[592,864]	[616,792]	[688,800]	[716,808]	[748,784]	[776,808]	[792,748]	[800,888]
	NDVI	[520,808]	[552,808]	[592,872]	[624,792]	[688,800]	[720,792]	[736,816]	[748,824]	[784,832]	[856,752]
	RVI	[512,808]	[536,808]	[576,800]	[632,816]	[685,840]	[700,856]	[744,864]	[776,872]	[784,856]	[792,880]
Tillering- Booting	DVI	[520,800]	[576,840]	[592,856]	[616,816]	[680,872]	[712,776]	[720,824]	[752,872]	[792,856]	[840,736]
	NDVI	[512,700]	[544,744]	[592,784]	[608,800]	[650,808]	[688,816]	[712,832]	[740,848]	[760,832]	[792,888]
	RVI	[504,872]	[552,832]	[624,800]	[664,808]	[692,864]	[716,872]	[748,880]	[776,848]	[792,880]	[840,672]
Jointing - Booting	DVI	[504,700]	[552,704]	[592,709]	[616,700]	[656,704]	[685,709]	[712,824]	[748,856]	[768,888]	[840,752]
	NDVI	[520,808]	[544,856]	[588,856]	[624,864]	[664,724]	[692,784]	[700,816]	[740,832]	[776,840]	[784,888]
	RVI	[512,816]	[560,864]	[592,872]	[635,816]	[664,856]	[700,824]	[768,724]	[784,808]	[792,840]	[816,856]
Tillering - Jointing - Booting	DVI	[520,536]	[600,685]	[650,588]	[752,800]	[776,840]	[752,888]	[688,704]	[680,712]	[808,748]	[848,744]
	NDVI	[528,685]	[568,760]	[696,768]	[692,880]	[760,700]	[768,664]	[784,700]	[800,504]	[800,685]	[888,504]
	RVI	[504,568]	[552,672]	[584,536]	[685,576]	[744,800]	[776,720]	[792,848]	[800,724]	[824,728]	[840,744]

Table 3
Potential textures.

Growth stage	Corresponding-band texture	Full-band texture
Tillering	MEA_{700} (-0.175)	CON_{588} (-0.439**), COR_{624} (0.614**), COR_{635} (0.497**), COR_{752} (0.420**), MEA_{656} (-0.680**)
Jointing	ENT_{776} (0.419**)	COR_{632} (-0.330*)
Booting	COR_{752} (0.607**)	COR_{596} (0.666**), SEM_{600} (0.775**)
Tillering-Jointing	SEM_{856} (-0.138)	COR_{632} (-0.029)
Tillering-Booting	MEA_{736} (0.552**), CON_{736} (-0.236*), DIS_{736} (-0.262*),COR_{736} (0.238*), MEA_{840} (0.683**)	COR_{504} (0.494**), SEM_{588} (0.507**), COR_{650}(0.478**), MEA_{672} (-0.644**), SEM_{752} (0.495**), HOM_{800} (0.383**)
Jointing-Booting	MEA_{724} (-0.223*), ENT_{724} (-0.377**), MEA_{768}(0.289**), MEA_{840} (0.325**)	COR_{576} (0.226*), COR_{588} (0.577**), MEA_{696} (-0.634**)
Tillering-Jointing-Booting	SEM_{748} (0.233*), MEA_{800} (0.488**) MEA_{808}(0.460**)	COR_{504} (0.444**), ENT_{536} (0.065), ENT_{584} (-0.289**), COR_{632} (0.166), COR_{635} (0.315**), COR_{650} (0.330**)

Note: Significance level: value* $<$ 0.05 means significant at 5%, value** $<$ 0.01 means significant at 1%, value *** $<$ 0.001 means significant at 0.1%.

dropping by 3.003% and 14.404% in the validation dataset when using models based on VI-CBT and VI-FBT, respectively. At the booting stage, the model using VI-CBT and VI-FBT declined the rRMSE by 11.434% and 15.310%, respectively, in the calibration dataset, and by 21.328% and 23.730%, respectively, in the validation dataset in the comparison with the model using VI.

In conclusion, the results shown that the combination of VI and FBT generated the highest level of improvement at the tillering stage, followed by the booting stage and jointing stage, while the combination of VI and CBT achieved the biggest improvements at the booting stage, followed by the tillering stage and jointing stage. The consistent changing trends of the evaluation parameters in the validation and calibration dataset demonstrated the excellent generalization ability of the models (Tables 5–8).

3.4. Evaluation of rice AGB models at multiple growth stages

Similar to the results of the single growth stage, the combination of VI and texture was also instructive to produce more satisfactory results than the pure VI at multiple growth stages (Fig. 6). The tillering-booting stages were in the greatest response to the involvement of texture, followed by the jointing-booting stages.

Compared to the monitoring accuracy achieved by the model using VI, the model using VI-CBT and VI-FBT individually declined the MAPE by 39.556% and 43.674% in the calibration dataset, and 24.242% and 27.922% in the validation dataset at the tillering-booting stages. At the jointing-booting stages, the models using VI-CBT and VI-FBT resulted in a decrease of rRMSE by 18.197% and 21.756%, respectively in the calibration dataset, and by 5.794% and 10.737%, respectively in the validation dataset.

By comparison, the tillering-jointing stages and the tillering-jointing-booting stages responded less sensitively to the involvement of textures. Among the two, the model using VI-CBT tended to achieve bigger progress at the tillering-jointing stages, while the model using VI-FBT generated a larger improvement at the tillering-jointing-booting stages. In the calibration dataset, the models using VI-CBT and VI-FBT declined the rRMSE by 2.070% and 16.718%, respectively at the tillering-jointing-booting stages, and decreased the rRMSE by 4.993% and 6.507%, respectively at the tillering-jointing stages (Tables 9–12).

The possible reasons why the VI-FBT models exhibited a relatively higher monitoring accuracy might be that the models based on VI-FBT covered a wider range of spectral bands than the models using VI-CBT and provided more valuable information strongly related to the rice AGB estimation (Xu et al., 2022b). The changes of each assessment

Table 4
Equations of the models.

Growth stage		Models
Tillering	I	$AGB = -1456.594 + 8091.291 \times NDVI_{(760,700)}$
	II	$AGB = -150.307 + 8876.68 \times NDVI_{(760,700)} - 431.78 \times MEA_{700}$
	III	$AGB = 8176.474 - 2988.855 \times NDVI_{(760,700)} + 12355.486 \times COR_{624} - 6018.136 \times COR_{635} - 1620.916 \times MEA_{656} - 6936.082 \times COR_{752}$
Jointing	I	$AGB = 398.367 + 52391.041 \times NDVI_{(776,748)}$
	II	$AGB = -388.501 + 50885.923 \times NDVI_{(776,748)} + 397.775 \times ENT_{776}$
	III	$AGB = 1117.442 + 50935.496 \times NDVI_{(776,748)} - 3026.044 \times COR_{632}$
Booting	I	$AGB = -4800.966 + 2674.527 \times RVI_{(752,700)}$
	II	$AGB = -4917.66 + 2218.871 \times RVI_{(752,700)} + 8302.928 \times COR_{752}$
	III	$AGB = -3201.352 + 2094.388 \times RVI_{(752,700)} + 6088.398 \times COR_{596}$
Tillering- Jointing	I	$AGB = -146.198 + 62922.818 \times NDVI_{(856,752)}$
	II	$AGB = 1742.403 + 65114.385 \times NDVI_{(856,752)} - 14229.036 \times SEM_{856}$
	III	$AGB = 220.05 + 69750.188 \times NDVI_{(856,752)} - 3426.471 \times COR_{632}$
Tillering- Booting	I	$AGB = -1535.542 - 61895.469 \times DVI_{(840,736)}$
	II	$AGB = 3875.924 - 141397.367 \times DVI_{(840,736)} + 361.52 \times MEA_{736} + 13583.206 \times COR_{736} - 837.23 \times MEA_{840}$
	III	$AGB = 685.219 - 43987.042 \times DVI_{(840,736)} + 3550.26 \times COR_{504} + 4435.54 \times COR_{650} - 504.73 \times MEA_{672}$
Jointing-Booting	I	$AGB = 42735.569 + 142314.213 \times DVI_{(840,752)} - 61719.527 \times RVI_{(768,724)}$
	II	$AGB = 30483.919 + 127650.041 \times DVI_{(840,752)} - 39136.431 \times RVI_{(768,724)} - 668.918 \times MEA_{724} + 512.16 \times MEA_{768} - 160.546 \times MEA_{840}$
	III	$AGB = 20712.742 + 32745.868 \times DVI_{(840,752)} - 25091.307 \times RVI_{(768,724)} + 3713.759 \times COR_{576} - 502.594 \times MEA_{696} + 2725.34 \times COR_{588}$
Tillering-Jointing-Booting	I	$AGB = 74367.154 - 108433.135 \times DVI_{(808,748)} - 79694.926 \times RVI_{(744,800)}$
	II	$AGB = 76025.147 - 107650.575 \times DVI_{(808,748)} - 79953.278 \times RVI_{(744,800)} - 8226.269 \times SEM_{748} + 389.704 \times MEA_{800} - 406.731 \times MEA_{808}$
	III	$AGB = 38762.457 - 20041.283 \times DVI_{(808,748)} - 45243.297 \times RVI_{(744,800)} + 4376.107 \times COR_{504} + 2554.066 \times ENT_{536} - 4311.195 \times COR_{632} + 5419.598 \times COR_{650}$

Table 5
Assessments of model performances for single growth stage from the perspective of R^2.

Stages	Calibration					Validation				
	Models			Model improvements		Models			Model improvements	
	I	II	III	I→II	I→III	I	II	III	I→II	I→III
Tillering	0.478	0.542	0.821	13.425%	71.685%	0.459	0.533	0.632	16.187%	37.603%
Jointing	0.569	0.571	0.663	0.422%	16.520%	0.496	0.517	0.565	4.133%	13.831%
Booting	0.583	0.673	0.701	15.415%	20.199%	0.639	0.850	0.861	33.130%	34.836%

Table 6
Assessments of model performances for single growth stage from the perspective of RMSE.

Stages	Calibration					Validation				
	Models			Model improvements		Models			Model improvements	
	I	II	III	I→II	I→III	I	II	III	I→II	I→III
Tillering	713.658	668.308	418.028	−6.355%	−41.425%	717.578	699.882	522.113	−2.466%	−27.239%
Jointing	775.200	772.988	685.482	−0.285%	−11.574%	1551.141	1530.920	1448.892	−1.304%	−6.592%
Booting	1193.452	1056.990	1010.730	−11.434%	−15.310%	1480.866	1165.028	1129.453	−21.328%	−23.730%

Table 7
Assessments of model performances for single growth stage from the perspective of rRMSE.

Stages	Calibration					Validation				
	Models			Model improvements		Models			Model improvements	
	I	II	III	I→II	I→III	I	II	III	I→II	I→III
Tillering	0.309	0.290	0.181	−6.355%	−41.425%	0.333	0.325	0.242	−2.466%	−27.239%
Jointing	0.178	0.178	0.157	−0.285%	−11.574%	0.359	0.354	0.335	−1.304%	−6.592%
Booting	0.166	0.147	0.140	−11.434%	−15.310%	0.202	0.159	0.154	−21.328%	−23.730%

Table 8
Assessments of model performances for single growth stage from the perspective of MAPE.

Stages	Calibration					Validation				
	Models			Model improvements		Models			Model improvements	
	I	II	III	I→II	I→III	I	II	III	I→II	I→III
Tillering	20.692	18.427	16.391	−10.947%	−20.785%	28.148	26.420	21.439	−6.140%	−23.836%
Jointing	12.651	12.486	12.123	−1.299%	−4.171%	29.219	28.341	25.010	−3.003%	−14.404%
Booting	14.679	12.535	12.033	−14.603%	−18.022%	17.837	14.875	13.950	−16.606%	−21.789%

Note:I represents the model using pure VI, II represents the model using VI-CBT and III represents the model using VI-FBT. I→II and I→III stand for the changing percentage of accuracy between varied models.

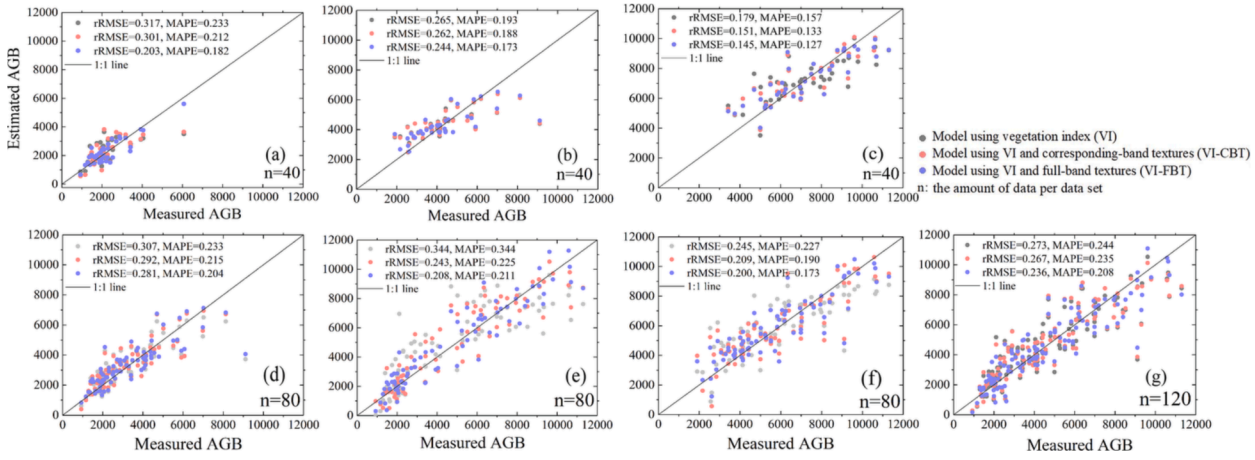

Fig. 6. Scatter plots of each model at different growth stages. (a) tillering, (b) jointing, (c) booting,(d) tillering-jointing, (e) tillering-booting, (f) jointing-booting, (g) tillering-jointing-booting stages.

Table 9
Assessments of model performances for multiple growth stages from the perspective of R^2.

Stages	Calibration					Validation				
	Model			Model improvement		Model			Model improvement	
	I	II	III	I→II	I→III	I	II	III	I→II	I→III
Tillering- Jointing	0.595	0.635	0.646	6.619%	8.550%	0.696	0.727	0.776	4.440%	11.523%
Tillering- Booting	0.730	0.891	0.921	22.061%	26.199%	0.637	0.766	0.818	20.147%	28.370%
Jointing - Booting	0.622	0.747	0.769	20.090%	23.545%	0.633	0.685	0.714	8.248%	12.814%
Tillering - Jointing - Booting	0.758	0.768	0.832	1.306%	9.773%	0.769	0.782	0.800	1.651%	4.018%

Table 10
Assessments of model performances for multiple growth stages from the perspective of RMSE.

Stages	Calibration					Validation				
	Model			Model improvement		Model			Model improvement	
	I	II	III	I→II	I→III	I	II	III	I→II	I→III
Tillering- Jointing	1059.714	1006.804	990.756	−4.993%	−6.507%	912.316	870.143	787.601	−4.623%	−13.670%
Tillering- Booting	1617.266	1028.174	874.511	−36.425%	−45.927%	1656.769	1348.430	1161.833	−18.611%	−29.874%
Jointing- Booting	1484.729	1214.557	1161.714	−18.197%	−21.756%	1281.118	1206.884	1143.558	−5.794%	−10.737%
Tillering- Jointing-Booting	1307.733	1280.666	1089.101	−2.070%	−16.718%	1155.680	1127.031	1086.920	−2.479%	−5.950%

Table 11
Assessments of model performances for multiple growth stages from the perspective of rRMSE.

Stages	Calibration					Validation				
	Model			Model improvement		Model			Model improvement	
	I	II	III	I→II	I→III	I	II	III	I→II	I→III
Tillering- Jointing	0.320	0.304	0.299	−4.993%	−6.507%	0.279	0.266	0.241	−4.623%	−13.670%
Tillering- Booting	0.342	0.218	0.185	−36.425%	−45.927%	0.346	0.282	0.243	−18.611%	−29.874%
Jointing - Booting	0.251	0.205	0.196	−18.197%	−21.756%	0.232	0.218	0.207	−5.794%	−10.737%
Tillering - Jointing - Booting	0.277	0.271	0.231	−2.070%	−16.718%	0.263	0.256	0.247	−2.479%	−5.950%

Table 12
Assessments of model performances for multiple growth stages from the perspective of MAPE.

Stages	Calibration					Validation				
	Model			Model improvement		Model			Model improvement	
	I	II	III	I→II	I→III	I	II	III	I→II	I→III
Tillering- Jointing	22.338	20.797	20.010	−6.900%	−10.423%	25.042	22.777	21.098	−9.048%	−15.753%
Tillering- Booting	36.373	21.986	20.488	−39.556%	−43.674%	30.813	23.343	22.209	−24.242%	−27.922%
Jointing - Booting	24.321	19.949	17.973	−17.974%	−26.102%	19.649	17.028	15.995	−13.342%	−18.600%
Tillering - Jointing - Booting	24.241	23.638	19.409	−2.487%	−19.935%	24.689	23.356	23.446	−5.402%	−5.035%

Note:I represents the model using pure VI, II represents the model using VI-CBT and III represents the model using VI-FBT. I→II and I→III stand for the changing percentage of accuracy between varied models.

parameter in the validation dataset showed a similar trend as in the calibration dataset with a slightly lower degree (Tables 9–12). The phenomenon illustrated that the combination of VI and texture beneficially favored the model accuracy, but there still existed further improvement space for the model stability at the multiple growth stages.

3.5. Evaluation of model performance under varied AGB levels

Based on the results presented in Section 3.4, further analysis was performed to explore the monitoring effects under varied AGB levels. The Jenks natural breaks, a kind of data classification approach, iteratively seeks to minimize the average deviation within classes and maximize the variance between different classes to gain the optimal arrangement of a set of values (Amirruddin et al., 2020), which was adopted to grade rice AGB. Three levels including high AGB, medium AGB and low AGB were set, and models using VI, VI-CBT and VI-FBT were tested on the values at different AGB levels.

Varied AGB levels had inconsistent responses to the incorporation of texture, and the models using VI-FBT exhibited more accurate estimates than VI-CBT and VI no matter under which AGB levels (Fig. 7). Model performances could be assumed to be equivalent if the improvement in accuracy was within five percent. Based on the principle, there were more possibilities for the accuracy of the extreme AGB levels (i.e. high AGB and low AGB) to be considerably optimized. At the tillering stage, the model using VI-CBT and VI-FBT declined the rRMSE of the low AGB level by 19.897% and 23.892%, respectively. AGB ranging from the low to medium level responded more sensitively to the involvement of texture at the jointing stage. No significant difference was observed at separate levels at the booting stage, which might attribute to the small amplitude of fluctuations in the AGB ranges during this period (Fig. 7).

Among the multiple growth stages, the combination of VI and FBT tended to lay more favorable effect at lower AGB levels. For example, the model using VI-FBT resulted in a decrease of rRMSE by 25.931% at the jointing-booting stages, 19.882% at the tillering-jointing-booting stages and 10.682% at the tillering-jointing stages, respectively. Compared to the model using VI, the highest level of improvement was achieved at the tillering-booting stages. The model using VI-CBT and VI-FBT improved the rRMSE of the low AGB by 42.762% and 51.075%,

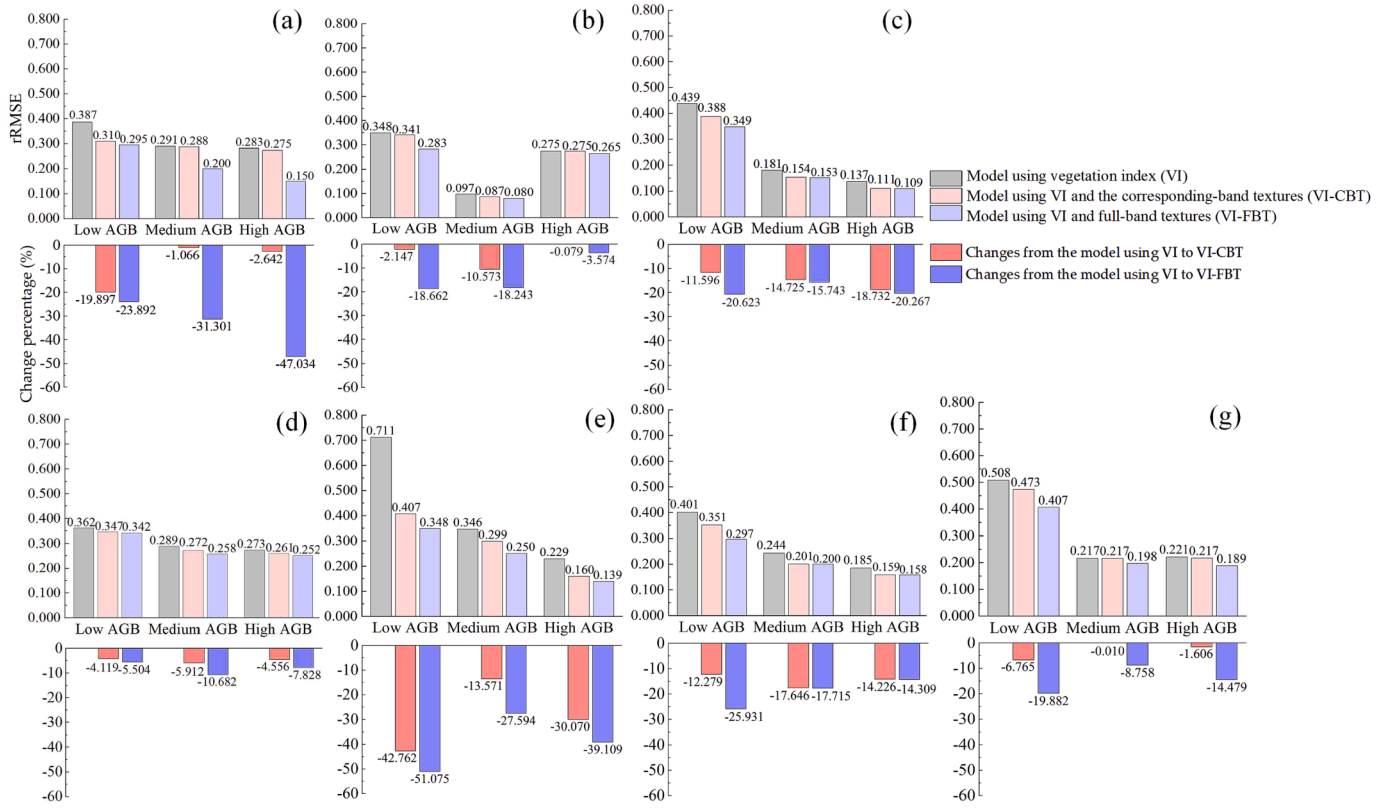

Fig. 7. The rRMSEs of estimation under varied AGB levels and the change percentage between models at different growth stages. (a) tillering, (b) jointing, (c) booting, (d) tillering-jointing, (e) tillering-booting, (f) jointing-booting, (g) tillering-jointing-booting stages.

respectively, during the period (Fig. 7(e)).

3.6. Comparing the accuracy of error values under varied models

To further understand the overestimation and underestimation in each model, the numerical difference between the measured AGB and the estimated AGB (D-value) was calculated. If the D-value was below zero, the value was grouped as underestimated, otherwise the model was regarded to overestimate the value.

At the tillering stage, the models using VI-CBT, VI-FBT improved the rRMSE of the overestimated values by 14.615% and 37.001%, respectively. At the jointing stage, the involvement of VI-CBT and VI-FBT resulted in a decrease in rRMSE by 5.189% and 18.017%, respectively on the overestimations. At the booting stage, the rRMSE exhibited the biggest improvement of 21.323% on the underestimation when using the model based on VI-FBT, and the improvement diversity on the overestimation between the model using VI-CBT and VI-FBT was not very great, with the respective decline of rRMSE of 11.748% and 13.256%.

At the tillering-jointing stages, the models using VI-CBT and VI-FBT separately decreased the rRMSE of the underestimated values by 9.301% and 12.509%. The combination of VI and FBT had the biggest improvement on the overestimations at the tillering-booting stages, with a decreasing level of rRMSE by 52.091%. At the jointing-booting stages,

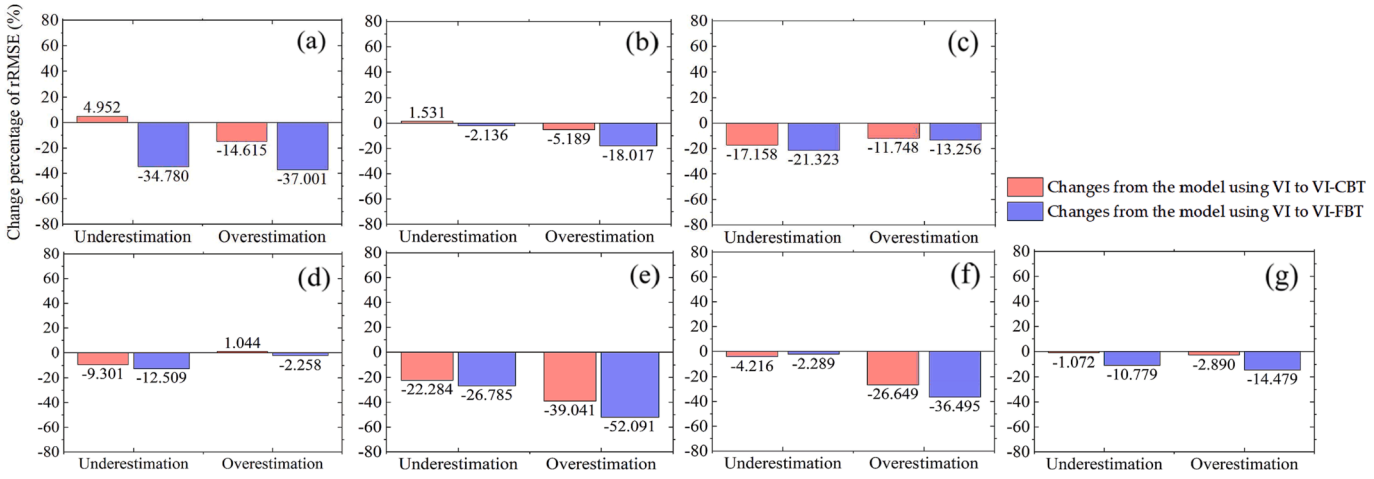

Fig. 8. Overestimations and underestimations in models at different growth stages. (a) tillering, (b) jointing, (c) booting, (d) tillering-jointing, (e) tillering-booting, (f) jointing-booting, (g) tillering-jointing-booting stages.

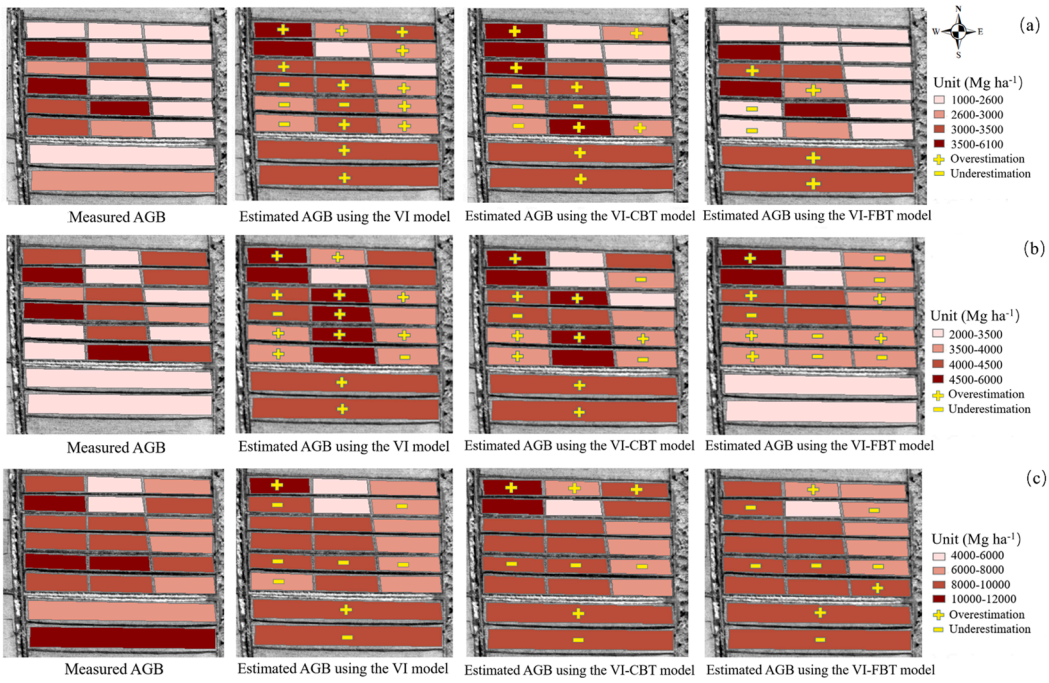

Fig. 9. Visualization of the measured AGB and estimated AGB at three single growth stages in 2018 using different models. (a) tillering, (b) jointing, (c) booting stage.

the model based on VI-CBT and VI-FBT improved the rRMSE of the overestimations by 26.649% and 36.495%, respectively. The model using VI-FBT declined the rRMSE of the underestimations by 10.779% and decreased the rRMSE of the overestimations by 14.479% at the tillering-jointing-booting growth stages (Fig. 8).

Fig. 9 shows the temporal and spatial variations of the measured AGB and estimated AGB of rice during the three growth stages in the experimental fields. It can be visually observed that the models using VI were more inclined to produce overestimations at the tillering and the jointing stage, and AGBs in several plots were underestimated at the booting stage. The number of overestimated values always declined with the involvement of texture, and the phenomenon was more obvious at the earlier stages of rice growth. The maps of AGB distribution can help farmers observe the AGB changes in each plot, providing guidance for the scientific fertilization to avoid field pollution such as water pollution (Xu et al., 2022b). If the observed AGB is low, appropriate nitrogen fertilizer needs to be supplied to promote the rice growth; if the AGB is high, no more nitrogen fertilizer should be continued to be applied to the field, preventing the negative impact caused by the excessive nitrogen fertilizer on rice growth and farmland ecological environment (Chen et al., 2005; Tao et al., 2014).

4. Discussion

4.1. The different responses of textures to AGB

The results show that the involvement of texture helped raise the monitoring accuracy of the rice AGB at different combinations of growth stages, which could be explained by the following reasons: First, the comprehensive relationship between VI and texture took the information of rice plants and soil into consideration simultaneously, reducing the interference of the background. Second, the combination of texture and VI increased the dimensionality of data, taking advantage of the spatial information as supplement, and compensated for the only spectral information contained in VI. Texture contains the information of the tonal variations of the images, which reflects the spatial traits of images (Haralick et al., 1973). In detail, textures described the spatial relationship between the crop communities through comparing the variability of gray-value between the target pixel and the adjacent neighbors (Liu et al., 2018). The morphology of canopy structure and organs dynamically changed in the rice growth cycle, in return resulting in the changing textures. Therefore, texture was also a good indicator of crop structure. As a result, using texture and VI together enhanced the discriminating capability to detect the crop structural transformation and the accumulation process of rice AGB.

Different textural features played inconsistent roles in monitoring crop growth. Lu et al. pointed out that MEA showed a similar changing trend with the spectral features, among them, MEA_{680}, MEA_{800} and MEA_{900} were highly correlated to rice potassium accumulation (Lu et al., 2021); Zheng et al. found that MEA_{550} and MEA_{800} played an important role for rice AGB estimation (Zheng et al., 2019); COR located in the green and red bands was found to perform well in the potato AGB models (Liu et al., 2022b). These results are similar to the phenomenon found in this study, where MEA and COR were two important textures for monitoring rice AGB. MEA could smooth the information in the moving windows, minimizing the influence of the background (Zheng et al., 2019) and COR could distinguish the textures of background and the rice plant by comparing the similarity of pixels gray-level (Haralick, 2019), making them become great variables for assisting the monitoring accuracy of VIs in rice AGB estimation.

4.2. The different responses of textures to AGB at varied growth stages

The quantitative results in Section 3 showed that the combination of texture and VI had different effects on AGB estimation at the varied combinations of growth stages: At the tillering stage, the plants did not form uniform canopies and the background with mixed soil and water brought noise to the reflectivity (Zheng et al., 2020b). Contrarily, the complex background embodied in the textures, highlighting the critical role of textures at the tillering stage (Xu et al., 2022b). Therefore, the involvement of texture generated a significant positive effect on the monitoring accuracy at this period. For instance, the model using VI-FBT yielded the greatest level of improvement in MAPE by 20.785% in the calibration dataset. During the tillering stage, the water surface covering

rice seedlings was like a mirror with little texture, making the seedlings with minor AGB too tiny to be identified. Consequently, it gave more possibilities for plants with larger AGB to be identified in the images, explaining why the high level of AGB possessed more sensitive response to the involvement of texture at the tillering stage (Fig. 7(a)).

At the jointing stage, the rice plants grew irregularly with the changing stems, bringing obstacles for VI and texture to capture the rapid change of canopy morphology (Wang et al., 2019; Zheng et al., 2020b). Compared to that of the tillering stage, the influence of the soil background gradually reduced due to the expanding leaf area, leading to the decline of the estimating capacity of texture at the jointing stage (Xu et al., 2022b). The models using VI-CBT and VI-FBT produced tiny improvements by 0.285% and 11.574% on rRMSE, respectively in the calibration dataset at the jointing stage. The relatively positive impact on lower AGB level during the jointing stage might attribute to the participation of ENT and COR in models. ENT representing the randomness of the involved textural information and COR reflecting the gray consistency of image both exerted more satisfactory effect to describe the chaotic growth of rice seedling with smaller AGBs.

The improvements when using model based on VI-FBT at the booting stage was relatively smaller than that at the tillering stage (Tables 5–8), indicating that texture showed a lower sensitivity to the AGB at the booting stage in comparison with the tillering stage. The phenomenon might be explained by the following reasons: First, the steady canopy structure gradually presented relatively constant reflectivity and texture at the booting stage (Chang et al., 2005). LAI approaching the highest level made the plant rows adjacent, minimizing the interference of the soil background (Duan et al., 2019). The role of texture reached its upper limitation of providing a comprehensive profile of AGB at booting stage. Second, only using COR at the booting stage might be less effective than using the diversity of textures including COR and MEA at the tillering stage. Compared to various red and red-edge bands in FBT at the tillering stage, the single texture (COR_{596}) located in yellow bands at the booting stage exhibited a relatively weaker correlation with rice AGB. Additionally, the underestimated values in the models using VI alone at the booting stage were probably related to the saturation problem, which meant that VIs no longer changed with the accumulation of AGB (Liu et al., 2022b). Models using VI-CBT and VI-FBT could help alleviate the saturation problem caused by the model using VI, and exerted positive effect the AGB error values as presented in Fig. 8(c) and Fig. 9.

Among the multiple growth stages, the tillering-booting stages obtained the greatest level of improvement of rRMSE by 36.425 % in the model using VI-CBT and 45.927% in the model using VI-FBT, respectively. The existence of the extreme values (i.e. the maximum and minimum AGB) in this dataset might help explain the phenomenon: First, the models always integrated the numerical traits of the AGB values floating around the average value of the dataset. Relatively less attention was paid to the traits of the extreme values in the modelling process (Coles and Powell, 1996). Therefore, more dimensional information such as texture in this study needed to be added into the modelling process to improve the predicting accuracy of the extreme values. Second, the extreme values located at both the ends of the fitting line always determined the stretching effect of the model fitting line, strongly influencing the monitoring accuracy (Hall and Weissman, 1997). These reasons could also help explain why the combination of VI and texture provided larger progress on the accuracy under the extreme levels of AGB at different combinations of growth stages (Fig. 7).

4.3. Outlook for future work

The study compared the performances of the AGB models using VI and texture at different combinations of growth stages. Future work will be performed on investigating the potential of using structural properties such as crop height and volume in estimating AGB (Liu et al., 2022a; Maimaitijiang et al., 2020; Xu et al., 2022a). The shortcomings of the UAV platform such as weak battery capacity, limited flying height, and restricted working time pose challenges for their application to large regions (Padro et al., 2019; Liu et al., 2022b). Improving the usability of UAVs is also an interesting topic. Satellite remote sensing can take wide-scope images periodically, and various current satellites such as RapidEye (Huang et al., 2017), Sentinel-2 (Dong et al., 2020) and WorldView (Sagan et al., 2021) equipped with red-edge bands possibly play potential critical roles in monitoring crop growth. Future studies will be conducted with experiments on exploring how to integrate the advantages of different types of platforms. Moreover, the applicability of the proposed models shall be examined in other geographic regions to assess their universality (Duan et al., 2021). More diverse VIs and advanced methods such as machine learning can be adopted in the subsequent research (Maimaitijiang et al., 2020; Agbulut et al., 2021).

5. Conclusion

The study evaluated the monitoring accuracy of using VI combined with CBT and FBT to estimate rice AGB at different combinations of growth stages and contributed a dynamic estimation scheme for rice AGB. The conclusions are as follows:

1. The combination of texture and VI provided instructive solutions to increase the monitoring accuracy of rice AGB at different combinations of growth stages, and the best performances were generated in the models using VI-FBT. Models using VI and texture always produced positive effect on the extreme AGB levels;
2. Textures had different responses to AGB during varied growth stages. Overall, the tillering stage responded most sensitively to the participation of texture, followed by the booting stage and the jointing stage. Compared to using VI, the monitoring effect was substantially improved when using the model based on VI-CBT at the booting stage, while the accuracy increased remarkably based on models using VI-FBT at the tillering stage. The improvement of the combination of VI and texture was not very significant at the jointing stage. Models using VI-CBT and VI-FBT both generated the highest level of improvement at the tillering-booting stages, followed by the jointing-booting stages.
3. VIs composed of near-infrared and red-edge bands gave light on rice AGB estimation, while yellow, green and red bands were good tools to estimate rice AGB in the spatial dimension. Textures such as MEA and COR had irreplaceable positions in the rice AGB estimation.

On the whole, the research provides valuable implications for precise management of rice AGB, which is helpful for officials and farmers to predict future rice yield and control field fertilization.

Declaration of Competing Interest

The authors declare that they have no known competing financial interests or personal relationships that could have appeared to influence the work reported in this paper.

Acknowledgements

This study was supported by the Ningbo Key Research and Development Program (2022Z159), National Natural Science Foundation of China (41871328) and the National Key Research and Development Plan of China (2016YFD0300601).

References

Agbulut, U., Gurel, A.E., Bicen, Y., 2021. Prediction of daily global solar radiation using different machine learning algorithms: evaluation and comparison. Renew. Sustain. Energy Rev. 135 https://doi.org/10.1016/j.rser.2020.110114.

Amirruddin, A.D., Muharam, F.M., Ismail, M.H., Ismail, M.F., Tan, N.P., Karam, D.S., 2020. Hyperspectral remote sensing for assessment of chlorophyll sufficiency levels in mature oil palm (Elaeis guineensis) based on frond numbers: Analysis of decision

tree and random forest. Comput. Electron. Agric. 169 https://doi.org/10.1016/j.compag.2020.105221.
Berard, G.M., Cloutis, E.A., Mann, P., 2017. Leaf reflectance and transmission properties (350–2500 nm): implications for vegetation indices. J. Near Infrared Spectrosc. 25, 138–144. https://doi.org/10.1177/0967033516686043.
Camps-Valls, G., Campos-Taberner, M., Moreno-Martinez, A., Walther, S., Duveiller, G., Cescatti, A., Mahecha, M.D., Munoz-Mari, J., Garcia-Haro, F.J., Guanter, L., Jung, M., Gamon, J.A., Reichstein, M., Running, S.W., 2021. A unified vegetation index for quantifying the terrestrial biosphere. Sci. Adv. 7 https://doi.org/10.1126/sciadv.abc7447.
Cao, Q., Miao, Y.X., Wang, H.Y., Huang, S.Y., Cheng, S.S., Khosla, R., Jiang, R.F., 2013. Non-destructive estimation of rice plant nitrogen status with Crop Circle multispectral active canopy sensor. Field Crop Res 154, 133–144. https://doi.org/10.1016/j.fcr.2013.08.005.
Chang, K.W., Shen, Y., Lo, J.C., 2005. Predicting rice yield using canopy reflectance measured at booting stage. Agron. J. 97, 872–878. https://doi.org/10.2134/agronj2004.0162.
Chao, Z.H., Liu, N., Zhang, P.D., Ying, T.Y., Song, K.H., 2019. Estimation methods developing with remote sensing information for energy crop biomass: a comparative review. Biomass Bioenergy 122, 414–425. https://doi.org/10.1016/j.biombioe.2019.02.002.
Chen, C., Ma, Y., Ren, G.B., Wang, J.B., 2022. Aboveground biomass of salt-marsh vegetation in coastal wetlands: sample expansion of in situ hyperspectral and Sentinel-2 data using a generative adversarial network. Remote Sens. Environ. 270 https://doi.org/10.1016/j.rse.2021.112885.
Chen, J., Tang, C., Sakura, Y., Yu, J., Fukushima, Y., 2005. Nitrate pollution from agriculture in different hydrogeological zones of the regional groundwater flow system in the North China Plain. Hydrgeol. J. 13, 481–492. https://doi.org/10.1007/s10040-004-0321-9.
Chierici, M., Signorini, S.R., Mattsdotter-Bjork, M., Fransson, A., Olsen, A., 2012. Surface water fCO(2) algorithms for the high-latitude Pacific sector of the Southern Ocean. Remote Sens. Environ. 119, 184–196. https://doi.org/10.1016/j.rse.2011.12.020.
Coles, S.G., Powell, E.A., 1996. Bayesian methods in extreme value modelling: a review and new developments. Int. Stat. Rev. 64, 119–136. https://doi.org/10.2307/1403426.
de Siqueira, F.R., Schwartz, W.R., Pedrini, H., 2013. Multi-scale gray level co-occurrence matrices for texture description. Neurocomputing 120, 336–345. https://doi.org/10.1016/j.neucom.2012.09.042.
Devia, C.A., Rojas, J.P., Petro, E., Martinez, C., Mondragon, I.F., Patino, D., Rebolledo, M. C., Colorado, J., 2019. High-throughput biomass estimation in rice crops using UAV multispectral imagery. J. Intell. Rob. Syst. 96, 573–589. https://doi.org/10.1007/s10846-019-01001-5.
Dong, T.F., Liu, J.G., Qian, B.D., He, L.M., Liu, J., Wang, R., Jing, Q., Champagne, C., McNairn, H., Powers, J., Shi, Y.C., Chen, J.M., Shang, J.L., 2020. Estimating crop biomass using leaf area index derived from Landsat 8 and Sentinel-2 data. ISPRS J. Photogramm. Remote Sens. 168, 236–250. https://doi.org/10.1016/j.isprsjprs.2020.08.003.
Duan, B., Liu, Y.T., Gong, Y., Peng, Y., Wu, X.T., Zhu, R.S., Fang, S.H., 2019. Remote estimation of rice LAI based on Fourier spectrum texture from UAV image. Plant Methods 15. https://doi.org/10.1186/s13007-019-0507-8.
Duan, B., Fang, S.H., Gong, Y., Peng, Y., Wu, X.T., Zhu, R.S., 2021. Remote estimation of grain yield based on UAV data in different rice cultivars under contrasting climatic zone. Field Crop. Res. 267 https://doi.org/10.1016/j.fcr.2021.108148.
Fang, M.H., Ju, W.M., Zhan, W.F., Cheng, T., Qiu, F., Wang, J., 2017. A new spectral similarity water index for the estimation of leaf water content from hyperspectral data of leaves. Remote Sens. Environ. 196, 13–27. https://doi.org/10.1016/j.rse.2017.04.029.
Fang, Q.Q., Wang, G.Q., Liu, T.X., Xue, B.L., A, y.l.,, 2018. Controls of carbon flux in a semi-arid grassland ecosystem experiencing wetland loss: vegetation patterns and environmental variables. Agric. For. Meteorol. 259, 196–210. https://doi.org/10.1016/j.agrformet.2018.05.002.
Freeman, K.W., Girma, K., Arnall, D.B., Mullen, R.W., Martin, K.L., Teal, R.K., Raun, W. R., 2007. By-plant prediction of corn forage biomass and nitrogen uptake at various growth stages using remote sensing and plant height. Agron. J. 99, 530–536. https://doi.org/10.2134/agronj2006.0135.
Fu, Y.Y., Yang, G.J., Song, X.Y., Li, Z.H., Xu, X.G., Feng, H.K., Zhao, C.J., 2021. Improved estimation of winter wheat aboveground biomass using multiscale textures extracted from UAV-based digital images and hyperspectral feature analysis. Remote Sens. (Basel) 13. https://doi.org/10.3390/rs13040581.
Guo, A.T., Huang, W.J., Dong, Y.Y., Ye, H.C., Ma, H.Q., Liu, B., Wu, W.B., Ren, Y., Ruan, C., Geng, Y., 2021. Wheat yellow rust detection using UAV-based hyperspectral technology. Remote Sens. (Basel) 13. https://doi.org/10.3390/rs13010123.
Haboudane, D., Miller, J.R., Pattey, E., Zarco-Tejada, P.J., Strachan, I.B., 2004. Hyperspectral vegetation indices and novel algorithms for predicting green LAI of crop canopies: Modeling and validation in the context of precision agriculture. Remote Sensing of Environment 90, 337-352.http://doi.org/10.1016/j.rse.2003.12.013.
Hall, P., Weissman, I., 1997. On the estimation of extreme tail probabilities. Ann. Stat. 25, 1311–1326.
Haralick, R.M., 2019. Dependence. Pattern Recogn. Lett. 124, 2–20. https://doi.org/10.1016/j.patrec.2017.12.008.
Haralick, R.M., Shanmugam, K., Dinstein, I., 1973. Textural features for image classification. IEEE Trans. Syst. Man Cybern. SMC3, 610–621. https://doi.org/10.1109/tsmc.1973.4309314.
Hsu, P.H., 2007. Feature extraction of hyperspectral images using wavelet and matching pursuit. ISPRS J. Photogramm. Remote Sens. 62, 78–92. https://doi.org/10.1016/j.isprsjprs.2006.12.004.
Huang, S.Y., Miao, Y.X., Yuan, F., Gnyp, M.L., Yao, Y.K., Cao, Q., Wang, H.Y., Lenz-Wiedemann, V.I.S., Bareth, G., 2017. Potential of RapidEye and WorldView-2 satellite data for improving rice nitrogen status monitoring at different growth stages. Remote Sens. (Basel) 9. https://doi.org/10.3390/rs9030227.
Inoue, Y., Penuelas, J., Miyata, A., Mano, M., 2008. Normalized difference spectral indices for estimating photosynthetic efficiency and capacity at a canopy scale derived from hyperspectral and CO2 flux measurements in rice. Remote Sens. Environ. 112, 156–172. https://doi.org/10.1016/j.rse.2007.04.011.
Jordan, C.F., 1969. Derivation of leaf-area index from quality of light on forest floor. Ecology 50, 663–1000. https://doi.org/10.2307/1936256.
Kokaly, R.F., Clark, R.N., 1999. Spectroscopic determination of leaf biochemistry using band-depth analysis of absorption features and stepwise multiple linear regression. Remote Sens. Environ. 67, 267–287. https://doi.org/10.1016/s0034-4257(98)00084-4.
Li, H.M., Lin, W.P., Pang, F.R., Jiang, X.P., Cao, W.X., Zhu, Y., Ni, J., 2020b. Monitoring wheat growth using a portable three-band instrument for crop growth monitoring and diagnosis. Sensors 20. https://doi.org/10.3390/s20102894.
Li, B., Xu, X.M., Zhang, L., Han, J.W., Bian, C.S., Li, G.C., Liu, J.G., Jin, L.P., 2020a. Above-ground biomass estimation and yield prediction in potato by using UAV-based RGB and hyperspectral imaging. ISPRS J. Photogramm. Remote Sens. 162, 161–172. https://doi.org/10.1016/j.isprsjprs.2020.02.013.
Li, S.Y., Yuan, F., Ata-Ui-Karim, S.T., Zheng, H.B., Cheng, T., Liu, X.J., Tian, Y.C., Zhu, Y., Cao, W.X., Cao, Q., 2019. Combining color indices and textures of UAV-based digital imagery for rice LAI estimation. Remote Sens. (Basel) 11. https://doi.org/10.3390/rs11151763.
Li, Z.H., Zhao, Y., Taylor, J., Gaulton, R., Jin, X.L., Song, X.Y., Li, Z.H., Meng, Y., Chen, P. F., Feng, H.K., Wang, C., Guo, W., Xu, X.G., Chen, L.P., Yang, G.J., 2022. Comparison and transferability of thermal, temporal and phenological-based in-season predictions of above-ground biomass in wheat crops from proximal crop reflectance data. Remote Sens. Environ. 273 https://doi.org/10.1016/j.rse.2022.112967.
Liu, Y., Feng, H.K., Yue, J.B., Jin, X.L., Li, Z.H., Yang, G.J., 2022a. Estimation of potato above-ground biomass based on unmanned aerial vehicle red-green-blue images with different texture features and crop height. Front. Plant Sci. 13 https://doi.org/10.3389/fpls.2022.938216.
Liu, Y., Feng, H.K., Yue, J.B., Li, Z.H., Yang, G.J., Song, X.Y., Yang, X.D., Zhao, Y., 2022b. Remote-sensing estimation of potato above-ground biomass based on spectral and spatial features extracted from high-definition digital camera images. Comput. Electron. Agric. 198 https://doi.org/10.1016/j.compag.2022.107089.
Liu, S.S., Li, L.T., Gao, W.H., Zhang, Y.K., Liu, Y.N., Wang, S.Q., Lu, J.W., 2018. Diagnosis of nitrogen status in winter oilseed rape (Brassica napus L.) using in-situ hyperspectral data and unmanned aerial vehicle (UAV) multispectral images. Comput. Electron. Agric. 151, 185–195. https://doi.org/10.1016/j.compag.2018.05.026.
Liu, J.G., Pattey, E., Miller, J.R., McNairn, H., Smith, A., Hu, B.X., 2010. Estimating crop stresses, aboveground dry biomass and yield of corn using multi-temporal optical data combined with a radiation use efficiency model. Remote Sens. Environ. 114, 1167–1177. https://doi.org/10.1016/j.rse.2010.01.004.
Liu, H.Y., Zhu, H.C., Li, Z.H., Yang, G.J., 2020. Quantitative analysis and hyperspectral remote sensing of the nitrogen nutrition index in winter wheat. Int. J. Remote Sens. 41, 858–881. https://doi.org/10.1080/01431161.2019.1650984.
Lu, J.S., Eitel, J.U.H., Engels, M., Zhu, J., Ma, Y., Liao, F., Zheng, H.B., Wang, X., Yao, X., Cheng, T., Zhu, Y., Cao, W.X., Tian, Y.C., 2021. Improving Unmanned Aerial Vehicle (UAV) remote sensing of rice plant potassium accumulation by fusing spectral and textural information. Int. J. Appl. Earth Obs. Geoinf. 104 https://doi.org/10.1016/j.jag.2021.102592.
Lu, G.L., Wang, D.S., Qin, X.L., Muller, S., Little, J.V., Wang, X., Chen, A.Y., Chen, G., Fei, B.W., 2019. Histopathology feature mining and association with hyperspectral imaging for the detection of squamous neoplasia. Sci. Rep. 9 https://doi.org/10.1038/s41598-019-54139-5.
Lucas, R., De Kerchove, R.V., Otero, V., Lagomasino, D., Fatoyinbo, L., Omar, H., Satyanarayana, B., Dahdouh-Guebas, F., 2020. Structural characterisation of mangrove forests achieved through combining multiple sources of remote sensing data. Remote Sens. Environ. 237 https://doi.org/10.1016/j.rse.2019.111543.
Lumia, R., Haralick, R.M., Zuniga, O., Shapiro, L., Pong, T.C., Wang, F.P., 1983. Texture analysis of aerial photographs. Pattern Recogn. 16, 39–46. https://doi.org/10.1016/0031-3203(83)90006-7.
Maimaitijiang, M., Sagan, V., Sidike, P., Daloye, A.M., Erkbol, H., Fritschi, F.B., 2020. Crop monitoring using satellite/UAV data fusion and machine learning. Remote Sens. (Basel) 12. https://doi.org/10.3390/rs12091357.
Meng, L., Wu, Y.F., Hu, X., Lu, G.H., Ren, D.C., Song, J.Q., 2017. Using hyperspectral data for detecting late frost injury to winter wheat under different topsoil moistures. Spectrosc. Spectr. Anal. 37, 1482–1488. https://doi.org/10.3964/j.issn.1000-0593(2017)05-1482-07.
Mukherjee, A., Misra, S., Raghuwanshi, N.S., 2019. A survey of unmanned aerial sensing solutions in precision agriculture. J. Netw. Comput. Appl. 148 https://doi.org/10.1016/j.jnca.2019.102461.
Nakaji, T., Kosugi, Y., Takanashi, S., Niiyama, K., Noguchi, S., Tani, M., Oguma, H., Nik, A.R., Kassim, A.R., 2014. Estimation of light-use efficiency through a combinational use of the photochemical reflectance index and vapor pressure deficit in an evergreen tropical rainforest at Pasoh, Peninsular Malaysia. Remote Sens. Environ. 150, 82–92. https://doi.org/10.1016/j.rse.2014.04.021.
Numata, I., Roberts, D.A., Chadwick, O.A., Schimel, J.P., Galvao, L.S., Soares, J.V., 2008. Evaluation of hyperspectral data for pasture estimate in the Brazilian Amazon using

field and imaging spectrometers. Remote Sens. Environ. 112, 1569–1583. https://doi.org/10.1016/j.rse.2007.08.014.
Padro, J.C., Munoz, F.J., Planas, J., Pons, X., 2019. Comparison of four UAV georeferencing methods for environmental monitoring purposes focusing on the combined use with airborne and satellite remote sensing platforms. Int. J. Appl. Earth Obs. Geoinf. 75, 130–140. https://doi.org/10.1016/j.jag.2018.10.018.
Prey, L., Schmidhalter, U., 2019. Simulation of satellite reflectance data using high-frequency ground based hyperspectral canopy measurements for in-season estimation of grain yield and grain nitrogen status in winter wheat. ISPRS J. Photogramm. Remote Sens. 149, 176–187. https://doi.org/10.1016/j.isprsjprs.2019.01.023.
Qiu, Z.C., Xiang, H.T., Ma, F., Du, C.W., 2020. Qualifications of rice growth indicators optimized at different growth stages using unmanned aerial vehicle digital imagery. Remote Sens. (Basel) 12. https://doi.org/10.3390/rs12193228.
Rouse, J.W., Haas, R.H., Schell, J.A., Deering, D.W., Harlan, J.C., 1974. Monitoring the vernal advancement of retrogradation of natural vegetation. NASA/GSFC, type III, final report. Greenbelt, MD.
Sagan, V., Maimaitijiang, M., Bhadra, S., Maimaitiyiming, M., Brown, D.R., Sidike, P., Fritschi, F.B., 2021. Field-scale crop yield prediction using multi-temporal WorldView-3 and PlanetScope satellite data and deep learning. ISPRS J. Photogramm. Remote Sens. 174, 265–281. https://doi.org/10.1016/j.isprsjprs.2021.02.008.
Seck, P.A., Diagne, A., Mohanty, S., Wopereis, M.C.S., 2012. Crops that feed the world 7: rice. Food Security 4, 7–24. https://doi.org/10.1007/s12571-012-0168-1.
Spiertz, J.H.J., Ewert, F., 2009. Crop production and resource use to meet the growing demand for food, feed and fuel: opportunities and constraints. Njas-Wageningen J. Life Sci. 56, 281–300. https://doi.org/10.1016/s1573-5214(09)80001-8.
Sun, H., Li, M.Z., Zhao, Y., Zhang, Y.E., Wang, X.M., Li, X.H., 2010. The spectral characteristics and chlorophyll content at winter wheat growth stages. Spectrosc. Spectr. Anal. 30, 192–196. https://doi.org/10.3964/j.issn.1000-0593(2010)01-0192-05.
Tao, Y.Y., Qu, H., Li, Q.J., Gu, X.H., Zhang, Y.N., Liu, M.J., Guo, L., Liu, J., Wei, J.J., Wei, G.J., Shen, K.R., Dittert, K., Lin, S., 2014. Potential to improve N uptake and grain yield in water saving Ground Cover Rice Production System. Field Crop. Res. 168, 101–108. https://doi.org/10.1016/j.fcr.2014.08.014.
Tucker, C.J., 1979. Red and photographic infrared linear combinations for monitoring vegetation. Remote Sens. Environ. 8, 127–150. https://doi.org/10.1016/0034-4257(79)90013-0.
Wang, F.L., Wang, F.M., Zhang, Y., Hu, J.H., Huang, J.F., Xie, J.K., 2019. Rice yield estimation using parcel-level relative spectra variables from UAV-based hyperspectral imagery. Front. Plant Sci. 10 https://doi.org/10.3389/fpls.2019.00453.
Wang, F.M., Yi, Q.X., Hu, J.H., Xie, L.L., Yao, X.P., Xu, T.Y., Zheng, J.Y., 2021. Combining spectral and textural information in UAV hyperspectral images to estimate rice grain yield. Int. J. Appl. Earth Obs. Geoinf. 102 https://doi.org/10.1016/j.jag.2021.102397.
Xu, T.Y., Wang, F.M., Xie, L.L., Yao, X.P., Zheng, J.Y., Li, J.L., Chen, S.T., 2022b. Integrating the textural and spectral information of UAV hyperspectral images for the improved estimation of rice aboveground biomass. Remote Sens. (Basel) 14. https://doi.org/10.3390/rs14112534.
Xu, T.Y., Wang, F.M., Yi, Q.X., Xie, L.L., Yao, X.P., 2022c. A bibliometric and visualized analysis of research progress and trends in rice remote sensing over the past 42 years (1980–2021). Remote Sens. (Basel) 14. https://doi.org/10.3390/rs14153607.
Xu, L., Zhou, L.F., Meng, R., Zhao, F., Lv, Z., Xu, B.Y., Zeng, L.L., Yu, X., Peng, S.B., 2022a. An improved approach to estimate ratoon rice aboveground biomass by integrating UAV-based spectral, textural and structural features. Precis. Agric. 23, 1276–1301. https://doi.org/10.1007/s11119-022-09884-5.
Yang, S.X., Feng, Q.S., Liang, T.G., Liu, B.K., Zhang, W.J., Xie, H.J., 2018. Modeling grassland above-ground biomass based on artificial neural network and remote sensing in the Three-River Headwaters Region. Remote Sens. Environ. 204, 448–455. https://doi.org/10.1016/j.rse.2017.10.011.
Yao, Y.K., Miao, Y.X., Cao, Q., Wang, H.Y., Gnyp, M.L., Bareth, G., Khosla, R., Yang, W., Liu, F.Y., Liu, C., 2014. In-season estimation of rice nitrogen status with an active crop canopy sensor. IEEE J. Sel. Top. Appl. Earth Obs. Remote Sens. 7, 4403–4413. https://doi.org/10.1109/jstars.2014.2322659.
Yokoyama, R., Haralick, R.M., 1978. Texture synthesis using a growth-model. Comput. Graphics Image Process. 8, 369–381. https://doi.org/10.1016/0146-664x(78)90063-1.
Yokoyama, R., Haralick, R.M., 1979. Texture pattern image generation by regular Markov-chain. Pattern Recogn. 11, 225–233. https://doi.org/10.1016/0031-3203(79)90033-5.
Yue, J.B., Yang, G.J., Tian, Q.J., Feng, H.K., Xu, K.J., Zhou, C.Q., 2019. Estimate of winter-wheat above-ground biomass based on UAV ultrahigh-ground-resolution image textures and vegetation indices. ISPRS J. Photogramm. Remote Sens. 150, 226–244. https://doi.org/10.1016/j.isprsjprs.2019.02.022.
Zhang, Z.H., 2016. Variable selection with stepwise and best subset approaches. Ann. Transl. Med. 4 https://doi.org/10.21037/atm.2016.03.35.
Zhang, Y., Hui, J., Qin, Q.M., Sun, Y.H., Zhang, T.Y., Sun, H., Li, M.Z., 2021. Transfer-learning-based approach for leaf chlorophyll content estimation of winter wheat from hyperspectral data. Remote Sens. Environ. 267 https://doi.org/10.1016/j.rse.2021.112724.
Zhao, K.G., Valle, D., Popescu, S., Zhang, X.S., Mallick, B., 2013. Hyperspectral remote sensing of plant biochemistry using Bayesian model averaging with variable and band selection. Remote Sens. Environ. 132, 102–119. https://doi.org/10.1016/j.rse.2012.12.026.
Zheng, H.B., Cheng, T., Li, D., Yao, X., Tian, Y.C., Cao, W.X., Zhu, Y., 2018. Combining unmanned aerial vehicle (UAV)-based multispectral imagery and ground-based hyperspectral data for plant nitrogen concentration estimation in rice. Front. Plant Sci. 9 https://doi.org/10.3389/fpls.2018.00936.
Zheng, H.B., Cheng, T., Zhou, M., Li, D., Yao, X., Tian, Y.C., Cao, W.X., Zhu, Y., 2019. Improved estimation of rice aboveground biomass combining textural and spectral analysis of UAV imagery. Precis. Agric. 20, 611–629. https://doi.org/10.1007/s11119-018-9600-7.
Zheng, H.B., Ma, J.F., Zhou, M., Li, D., Yao, X., Cao, W.X., Zhu, Y., Cheng, T., 2020a. Enhancing the nitrogen signals of rice canopies across critical growth stages through the integration of textural and spectral information from unmanned aerial vehicle (UAV) multispectral imagery. Remote Sens. (Basel) 12. https://doi.org/10.3390/rs12060957.
Zheng, H.B., Zhou, X., He, J.Y., Yao, X., Cheng, T., Zhu, Y., Cao, W.X., Tian, Y.C., 2020b. Early season detection of rice plants using RGB, NIR-G-B and multispectral images from unmanned aerial vehicle (UAV). Comput. Electron. Agric. 169 https://doi.org/10.1016/j.compag.2020.105223.
Zhou, X., Zheng, H.B., Xu, X.Q., He, J.Y., Ge, X.K., Yao, X., Cheng, T., Zhu, Y., Cao, W.X., Tian, Y.C., 2017. Predicting grain yield in rice using multi-temporal vegetation indices from UAV-based multispectral and digital imagery. ISPRS J. Photogramm. Remote Sens. 130, 246–255. https://doi.org/10.1016/j.isprsjprs.2017.05.003.